Int. J. Solids Structures Vol. 31, No. 2, pp. 145–168, 1994
Printed in Great Britain

0020–7683/94 $6.00+ .00

COMPUTATIONAL ANALYSIS OF DYNAMIC CRACK PROPAGATION ALONG A BIMATERIAL INTERFACE

C. Y. Lo, T. Nakamura and A. Kushner
Department of Mechanical Engineering, State University of New York at Stony Brook, NY 11794, U.S.A.

(*Received* 30 *April* 1993, *in revised form* 15 *July* 1993)

Abstract—Several features of the characteristics of a crack dynamically propagating along a bimaterial interface are investigated and their results are presented in this paper. The stress intensity factors of interface crack dynamics are accurately extracted from finite element field solutions using a new conservation integral. This integral is based on the steady-state solution for a dynamically propagating interface crack. It extracts the Mode I and II contributions of the mixed-mode crack-tip field. The ratio of the mixed-mode factors, or the phase angle is an essential parameter in defining the fracture resistance of dynamic interface cracks. A computational analysis is carried out for an interface crack in an infinite plane under either remote tensile or shear loading. The phase angle and the energy release rate of the growing interface crack with different crack-tip velocities are obtained for several bimaterial combinations. For a short time after the initiation of a growth, the energy release rate and the phase angle are found to be very sensitive to the crack-tip velocity. They are much less sensitive to the mismatch in bimaterial properties. At late time, the phase angle merges closer to the corresponding quasi-static values. A toughness formula based on critical energy release rate is proposed for the dynamic interface crack. This toughness criterion is implemented in a newly developed iterative procedure for computing crack propagation. With this procedure, the simulation of crack propagation exactly follows the condition specified by the toughness function. No artificial input or prior knowledge of the crack-tip velocity history is necessary. This is an effective method which can be used to interpret experimental data. We have employed this iterative technique in the simulation of published data for dynamic interface crack propagation to identify a correct toughness formula. The analysis shows that the resulting velocity history agrees well with the experimental record when appropriate parameters are chosen for the proposed toughness criterion.

1. INTRODUCTION

The need for a better understanding of interface fracture mechanics increases as the use of composite materials in engineering structures increases. In many applications, the composites may be subjected to dynamic loading or their failure mechanisms may involve dynamic characteristics. Some fundamental features of dynamic interface cracks have been discussed by Willis (1971) and more recently by Yang *et al.* (1991). However analytical solutions under these conditions are extremely difficult to obtain due to the complexity of the problems. Thus a computational method is essential for investigating the various features of dynamic crack propagation along bimaterial interfaces. To characterize dynamic failure behavior in composites, it is necessary to develop well-defined procedures for extracting the essential characteristics of the fracture process.

In this study, we establish a procedure to extract the mixed-mode stress intensity factors of dynamically moving interface cracks from numerically calculated field solutions. Experimental studies have shown that the ratio of Mode I to Mode II is important for interpretation of the dynamic interface toughness. The stress intensity factors are computed using specially formulated conservation integrals. Along with the energy release rate which is determined with a separate integral, these factors are critical in understanding the interface resistance to fracture. We also introduce an iterative method to simulate crack propagation along a bimaterial interface. This is an extension of a method introduced by Nakamura and Lo (1991) where an implicit scheme was used to propagate the crack through a homogeneous material. The current method accounts for more complex mixed-mode effects which are inherently present in the interface fracture field. In addition, a proper procedure to propagate the crack tip using a node release technique in a full-plane bimaterial geometry, and an accurate method to determine the energy release rate and the stress intensity factors during the node release are described.

Two types of dynamic interface crack growth are investigated in this work. First, we simulate the initiation and propagation of an initially finite length crack in an infinite medium (Griffith type crack) subjected to a static remote tensile or shear load. The full-field finite element analyses are carried out with various crack-tip velocities. The computed field solutions are used to determine the dynamic energy release rate and Mode I and II stress intensity factors. These fracture parameters are obtained with the domain integral formulations, The phase angle is also determined from the ratio of the stress intensity factors. Special attention is given to the transient behavior of both the energy release state and the phase angle as the crack begins to propagate along the interface. In the second case, we simulate a dynamic fracture testing carried out by Tippur and Rosakis (1991) where a pre-cracked three-point-bend bar was loaded to fracture by means of dynamic impact loading. Here, we propose dynamic crack growth criteria which govern the crack propagation process. The main purpose is to illustrate how a postulated toughness criterion can be determined using the iterative crack growth procedure. Several criteria are tested and their resulting crack-tip velocities are compared to the experimental measurements given by Tippur and Rosakis (1991). The transient behavior of the energy release rate and the phase angle are also characterized in detail.

2. DETERMINATION OF DYNAMIC INTERFACE K

2.1. *Crack-tip integral for dynamic interface crack*

Based on the fundamental crack-tip integral, the energy release rate $\mathscr{G}$ of an elastic two-dimensional solid under dynamic conditions with a crack moving along the x_1-direction is

$$\mathscr{G} = \lim_{\Gamma \to 0} \int_{\Gamma} \left[(W+T)n_1 - \sigma_{ij} \frac{\partial u_i}{\partial x_1} n_j \right] \mathrm{d}\Gamma, \tag{1}$$

where the integrating path Γ is an arbitrary contour surrounding a crack tip. The outward normal unit vector of Γ is denoted by n_j. Also σ_{ij} and u_i are Cartesian components of stresses and displacements, respectively, W is the strain energy density and T is the kinetic energy density at a material point. The above expression expresses the instantaneous energy release rate for any crack configuration, including interface cracks, as long as the limiting process is preserved. Under a steady-state crack growth condition and if the material properties are constant along the x_1-direction, the integral becomes path independent.

For a static elastic interface crack under a mixed-mode condition, an effective method was introduced by Shih and Asaro (1988) to determine each stress intensity factor from known field quantities. The extraction of these factors is important since the experimental results show that the toughness of an interface depends highly on the ratio of shear to tensile modes. The method is based on the linearity of material behavior and it uses a so-called 'interaction integral' with an auxiliary field which is a solution to a crack problem under some arbitrary loads. Similar methods have also been used to extract the three-dimensional stress intensity factors (Nakamura, 1991) and T-stress (Kfouri, 1986; Nakamura and Parks, 1992). Here the method is extended to extract the stress intensity factors of dynamically propagating interface cracks. As compared with the static case, the dynamic procedure is significantly more difficult. It requires an accurate method to propagate the crack and the auxiliary field itself is very complex. In the following, we describe how the new interaction integral based on the conservation law of elasticity is derived.

We begin by considering two separate fields. The first one comprises the actual field quantities, u_i, σ_{ij}, ε_{ij}. W, T of the dynamic interface crack problem whose unknown stress intensity factors are sought. The second one comprises auxiliary field quantities u_i^{aux}, $\sigma_{ij}^{\mathrm{aux}}$, $\varepsilon_{ij}^{\mathrm{aux}}$, W^{aux}, T^{aux} whose stress intensity factors are already known. Usually, they are solutions to an interface crack problem under some specific loading condition. Suppose we superimpose the actual and auxiliary fields, the resulting superimposed field quantities may be denoted as u_i^{sup}, $\sigma_{ij}^{\mathrm{sup}}$, $\varepsilon_{ij}^{\mathrm{sup}}$, W^{sup}, T^{sup}. Note the superimposed displacements, stresses and

strains are the simple sum of the two fields while the energy densities W^{sup} and T^{sup} are not. The energy release rates associated with the auxiliary and superimposed fields can be expressed as

$$\mathcal{G}^{aux} = \lim_{\Gamma \to 0} \int_{\Gamma} \left[(W^{aux} + T^{aux}) n_1 - \sigma_{ij}^{aux} \frac{\partial u_i^{aux}}{\partial x_1} n_j \right] d\Gamma, \tag{2}$$

$$\mathcal{G}^{sup} = \lim_{\Gamma \to 0} \int_{\Gamma} \left[(W^{sup} + T^{sup}) n_1 - \sigma_{ij}^{sup} \frac{\partial u_i^{sup}}{\partial x_1} n_j \right] d\Gamma. \tag{3}$$

The energy release rate of the actual field is already shown in (1). Using correct relations between the energy densities and after some algebra, the relationship between three energy release rates is given as

$$\mathcal{G}^{sup} = \mathcal{G} + \mathcal{G}^{aux} + I, \tag{4}$$

where I is the interaction or conservation integral and is given as

$$I = \lim_{\Gamma \to 0} \int_{\Gamma} \left[\left(\sigma_{ij} \varepsilon_{ij}^{aux} + \rho \frac{\partial u_i}{\partial t} \frac{\partial u_i^{aux}}{\partial t} \right) n_1 - \left(\sigma_{ij} \frac{\partial u_i^{aux}}{\partial x_1} + \sigma_{ij}^{aux} \frac{\partial u_i}{\partial x_1} \right) n_j \right] d\Gamma. \tag{5}$$

Here ρ is the mass density of the material. This integral, the difference between $\mathcal{G}^{sup}$ and the sum of $\mathcal{G}$ and $\mathcal{G}^{aux}$, is used to determine the stress intensity factors of the actual field as discussed in the next section.

2.2. *Extraction of dynamic stress intensity factors*

Using the dynamic interaction integral (5) and the relationship between the energy release rate and the dynamic stress intensity factors, one can effectively extract Mode I and Mode II stress intensity factors. The relation between energy release rate $\mathcal{G}$ and stress intensity factors for the dynamic interface crack is given in Yang *et al.* (1991) as

$$\mathcal{G} = \frac{\mathcal{F}}{4\mu_1} |\mathbf{K}|^2 = \frac{H_{22}}{4 \cosh^2 (\pi \varepsilon)} |\mathbf{K}|^2, \qquad \text{where } \mathbf{K} = K_I + iK_{II}. \tag{6}$$

Here $\mathcal{F}$ is the energy factor, μ_1 is the shear modulus of the upper plane and $\mathbf{K}$ is the complex stress intensity factor ($i = \sqrt{-1}$), which is a common expression used in the study interface fracture mechanics. The energy factor depends on the crack-tip velocity as well as the material constants. Also H_{22} is a component of the so-called "hermitian matrix" discussed in the next section. It reduces to $H_{22} = 4/E^*$ under a static condition with an interface crack between two different isotropic solids. Here E^* is the effective plane strain tensile modulus defined as

$$\frac{1}{E^*} = \frac{1}{2} \left(\frac{1 - v_1^2}{E_1} + \frac{1 - v_2^2}{E_2} \right). \tag{7}$$

The subscripts "1" and "2" in the Young's modulus E and the Poisson's ratio v indicate the upper and lower materials of the interface, respectively.

The following procedures demonstrate how the real and imaginary part of the complex stress intensity factor of the actual field can be extracted. First, we consider the previously described auxiliary field. The sum of the stress intensity factors of actual field $\mathbf{K}$ and the auxiliary field $\mathbf{K}^{aux}$ is the stress intensity factor of the superimposed field $\mathbf{K}^{sup}$. With (6), the relationship among the energy release rates and the stress intensity factors may be given as

$$\mathcal{G}^{\sup} = \frac{H_{22}}{4\cosh^2(\pi\varepsilon)}|\mathbf{K}^{\sup}|^2 = \frac{H_{22}}{4\cosh^2(\pi\varepsilon)}|\mathbf{K}^{\text{aux}}+\mathbf{K}|^2$$

$$= \mathcal{G}+\mathcal{G}^{\text{aux}}+\frac{H_{22}}{2\cosh^2(\pi\varepsilon)}(K_{\text{I}}K_{\text{I}}^{\text{aux}}+K_{\text{II}}K_{\text{II}}^{\text{aux}}). \tag{8}$$

Comparing (4) and (8) gives the following equation relating the dynamic interaction integral I to the stress intensity factors of the actual and auxiliary fields:

$$I = \frac{H_{22}}{2\cosh^2(\pi\varepsilon)}(K_{\text{I}}K_{\text{I}}^{\text{aux}}+K_{\text{II}}K_{\text{II}}^{\text{aux}}). \tag{9}$$

This is the fundamental equation which connects the computable interaction integral I shown in (5) to the unknown stress intensity factors of the dynamic interface crack **K**. The idea here is to choose two suitable auxiliary fields whose complete field quantities, including $K_{\text{I}}^{\text{aux}}$ and $K_{\text{II}}^{\text{aux}}$, are known *a priori*. Then, once two interaction integrals with respective auxiliary fields are computed, the unknown K_{I} and K_{II} of the actual field can be calculated.

Suitable choices for auxiliary fields are analytical solutions which give either pure Mode I or Mode II fields. Furthermore, since the asymptotic singular K-fields have the simplest form, these are usually selected as the auxiliary fields. The K-field solutions for the dynamic interface crack were recently obtained by Yang *et al.* (1991). The details of the asymptotic solutions and implementation of the auxiliary fields for I are described in Sections 2.3 and 4.1, respectively.

2.3. *Asymptotic singular crack-tip field*

Under dynamic conditions, the asymptotic solutions are functions of the instantaneous crack-tip speed. In general, the size of the crack-tip region dominated by the asymptotic singular field is smaller than that of a stationary crack. This aspect and the effect of higher order terms in homogeneous materials were recently discussed by Freund and Rosakis (1992). The steady state or the singular fields close to the tip of a crack moving along the interface of two anisotropic elastic solids is given by Yang *et al.* (1991). They used Stroh's (1962) steady-state formulation as a basis for deriving the solution. Their study shows that, within a K-dominated zone, the crack-tip field consists of a coupled in-plane oscillatory field characterized by a complex stress intensity factor and a non-oscillatory out-of-plane field characterized by a real stress intensity factor. The latter field corresponds to the Mode III deformation and is not accounted for here.

The asymptotic field of the dynamic interface crack can be conveniently characterized by the compliance-like hermitian matrix **H**. Directing attention to the in-plane deformation of a crack moving along the interface of two different isotropic solids with a crack-tip velocity v, the matrix **H** can be reduced to the following 2×2 complex variable matrix:

$$\mathbf{H} = \begin{bmatrix} \dfrac{\zeta_1(1-\zeta_1^2)}{\mu_1 D_1}+\dfrac{\zeta_2(1-\zeta_2^2)}{\mu_2 D_2} & i\left(\dfrac{1+\zeta_1^2-2\xi_1\zeta_1}{\mu_1 D_1}-\dfrac{1+\zeta_2^2-2\xi_2\zeta_2}{\mu_2 D_2}\right) \\ -i\left(\dfrac{1+\zeta_1^2-2\xi_1\zeta_1}{\mu_1 D_1}-\dfrac{1+\zeta_2^2-2\xi_2\zeta_2}{\mu_2 D_2}\right) & \dfrac{\xi_1(1-\zeta_1^2)}{\mu_1 D_1}+\dfrac{\xi_2(1-\zeta_2^2)}{\mu_2 D_2} \end{bmatrix}, \tag{10}$$

where $\xi_\alpha = \sqrt{1-(v/c_{\text{L}}^\alpha)^2}$, $\zeta_\alpha = \sqrt{1-(v/c_{\text{S}}^\alpha)^2}$, $D_\alpha = 4\xi_\alpha\zeta_\alpha-(1-\zeta_\alpha^2)^2$, μ_α is the shear modulus, and v is the crack-tip velocity. Also c_{L}^α and c_{S}^α are the longitudinal and shear wave speeds, respectively. Here α indicates for the upper ($\alpha = 1$) and lower ($\alpha = 2$) materials. The components of the above matrix are used to define the crack-tip solution.

The asymptotic stresses within the K-dominated zone can be expressed in the following form:

$$\sigma_{ij}(r,\theta;\varepsilon)=\frac{\mathrm{Re}\,[\mathbf{K}r^{i\varepsilon}]}{\sqrt{2\pi r}}\tilde{\sigma}_{ij}^{\mathrm{I}}(\theta;\varepsilon)+\frac{\mathrm{Im}\,[\mathbf{K}r^{i\varepsilon}]}{\sqrt{2\pi r}}\tilde{\sigma}_{ij}^{\mathrm{II}}(\theta;\varepsilon), \tag{11}$$

where r, θ are polar coordinates with their origins located at the moving crack tip and $\tilde{\sigma}_{ij}^{\mathrm{I}}$ and $\tilde{\sigma}_{ij}^{\mathrm{II}}$ are dimensionless angular functions. The explicit forms of these functions are given in Yang *et al.* (1991). Also ε is the oscillatory index defined with Dundur's parameter β as

$$\varepsilon=\frac{1}{2\pi}\ln\frac{1-\beta}{1+\beta},\qquad \text{where } \beta=\frac{-H_{12}}{\sqrt{H_{11}H_{22}}}. \tag{12}$$

Here, H_{11}, H_{22} and H_{12} are components in matrix $\mathbf{H}$ (10). Unlike the static case, the oscillatory index ε under dynamic conditions depends not only on the material mismatch but also on the *instantaneous* crack-tip velocity v. It is important to note that even for some bimaterial combinations for which $\varepsilon=0$ in the static case, ε is non-zero under dynamic conditions ($v>0$). This means the oscillatory behavior exists in the dynamic crack-tip field for all bimaterial combinations except the homogeneous case. As in the static case, the unit of the stress intensity factors contains an imaginary number when $\varepsilon\neq 0$.

An important parameter in defining the fracture toughness or the critical energy release rate is the phase angle. It is essentially the ratio of the shear to normal traction ahead of the crack which varies with the distance from the tip due to the oscillatory nature of the field. Thus, the phase angle must be defined in terms of a characteristic length scale L as

$$\psi(L)=\tan^{-1}\left\{\frac{\mathrm{Im}\,[\mathbf{K}L^{i\varepsilon}]}{\mathrm{Re}\,[\mathbf{K}L^{i\varepsilon}]}\right\}=\tan^{-1}\left\{\left(\frac{\sigma_{12}}{\eta\sigma_{22}}\right)_{r=L}\right\}. \tag{13}$$

Here η is a traction resolution factor, $\eta=\sqrt{H_{22}/H_{11}}$. This factor has a small dependence on the material properties and it increases monotonically with v, as shown in Fig. 5 of Yang *et al.* (1991). We note that the stress intensity factors in (13) do not reduce to the classically defined dynamic stress intensity factors for an isotropic homogeneous material since $\eta\neq 1$ even for a homogeneous crack. This discrepancy arises because the angular functions $\tilde{\sigma}_{ij}$ shown in (11) do not degenerate to the ones shown by Freund (1990) for the homogeneous case. Since the phase angle (13) is a function of length, when the distance changes from L_1 to L_2, the difference of the two phase angles is

$$\Delta\psi=\psi(L_2)-\psi(L_1)=\varepsilon\ln\left(\frac{L_2}{L_1}\right). \tag{14}$$

In the static case, where ε is generally very small, this difference remains relatively small. However, ε can be very large in the dynamic case, especially at a high crack-tip speed. Consequently $\Delta\psi$ can be quite large, and the choice of L must be made more carefully in the dynamic interface crack.

3. DYNAMIC INTERFACE CRACK GROWTH CONDITION

3.1. *Growth criteria*

It is useful to establish a toughness formula for a dynamically propagating interface crack. Such a formula will help in interpreting experimental data. Accurate determination of fracture parameters is quite difficult for dynamic interface crack experiments. We postulate that a criterion for crack propagation can be solely controlled by the instantaneous energy release rate. Then, a continuous growth is possible if the driving force $\mathcal{G}$ is at least equal to the dynamic fracture toughness. Physically, the dynamic fracture toughness of an interface crack $\mathcal{G}_{\mathrm{D}}$ may depend on several factors. We assume $\mathcal{G}_{\mathrm{D}}$ is given as a function of the instantaneous crack-tip velocity and the phase angle. Under these conditions, crack propagation is expressed as, $\mathcal{G}=\mathcal{G}_{\mathrm{D}}(v,\psi)$. There has been limited experimental work in

this area, and no accurate data exist for the toughness of dynamic interface cracks. Lacking empirical correlation, the growth criterion proposed here is based on a superposition of formulae for the static interface crack and the dynamic homogeneous crack. The accuracy of the proposed formula cannot be determined without sufficient experimental data. Nonetheless the formula should help to interpret the future experimental measurements, and demonstrate its accuracy by coherency of its ability to fit the data.

Many static experiments on the bimaterial interface have shown that the interface fracture toughness depends strongly on the mode mixity or the phase angle of the crack-tip field. Toughness has been observed to increase as the shearing mode increases in the crack-tip region. This is partly explained by the larger frictional contact of the crack faces. Hutchinson and Suo (1991) suggested a formula for the interface toughness with a parameter λ,

$$\mathscr{G}_c(\psi;\lambda) = \frac{\mathscr{G}_c^*}{1+(\lambda-1)\sin^2\psi}. \tag{15}$$

Here $\mathscr{G}_c^*$ is the reference toughness under $\psi = 0°$. When $\lambda = 0$ is chosen, the interface toughness is determined by the critical interface hoop stress. For $\lambda = 1$, the interface is ideally brittle and the mixed mode fracture toughness $\mathscr{G}_c$ is equal to $\mathscr{G}_c^*$ independent of the phase angle. Hutchinson and Suo (1991) have indicated $\lambda = 0.3$ fits well the experimental measurements of epoxy/glass interface and we have chosen this value for the analysis shown in Section 6. Other formulae also exist but their essential features are similar to (15).

There have been many experimental analyses of dynamic crack propagation in a homogeneous solid. Several empirically based formulae have been introduced for the dynamic toughness. In general, their measurements show the fracture toughness to increase under higher crack-tip velocity [see for example, Kobayashi and Dally (1979), Rosakis *et al.* (1984) and Ravi-Chandar and Knauss (1984)]. Theoretically, the limiting or the upper bound of the crack-tip velocity $v_{\lim}$ is the Rayleigh wave speed c_R for the homogeneous material, although the maximum velocity observed in most experiments is well below c_R except for tests under extremely high rate loading conditions (Ravichandran and Clifton, 1989). Many of the proposed formulae are similar, but there is yet to be a unified formula for various materials. Here we choose the following function for the dynamic toughness:

$$\mathscr{G}_D(v;\gamma) = \mathscr{G}_{Id}(1-v/v_{\lim})^{-\gamma}, \tag{16}$$

where $\mathscr{G}_{Id}$ is a constant and can be regarded as the initiation toughness under Mode I loading. The effects of loading rate are not taken into account in the above formula. The parameter γ can be varied to optimize the function to the experimentally observed fracture toughness of a dynamically growing crack. It allows the formula to cover a wide range of materials. This function models the theoretically infinite energy release rate required for the crack tip travelling at the limiting velocity $v_{\lim}$ when $\gamma > 0$. If $\gamma = 0$ is chosen, the toughness is constant and independent of crack-tip velocity. In a homogeneous material, the limiting velocity is taken as the Rayleigh wave speed, $v_{\lim} = c_R$. For $\gamma = 1$, the above function represents a close approximation to a universal function which relates the static energy release rate to the dynamic energy release rate [see Freund (1990)].

Although no detailed measurement has been made for the dynamic interface crack, we postulate a combination of the two formulae (15), (16) as a possible toughness criterion. The proposed criterion is expressed as

$$\mathscr{G}_D(v,\psi;\lambda,\gamma) = \frac{\mathscr{G}_d^*(1-v/v_{\lim})^{-\gamma}}{1+(\lambda-1)\sin^2\psi}, \tag{17}$$

where $\mathscr{G}_d^*$ can be regarded as the dynamic crack initiation toughness when $\psi = 0°$. Since no extensive data exist for the dynamic interface crack, the above function is only a candidate for the toughness formula. Other forms of the function which represent similar relationships

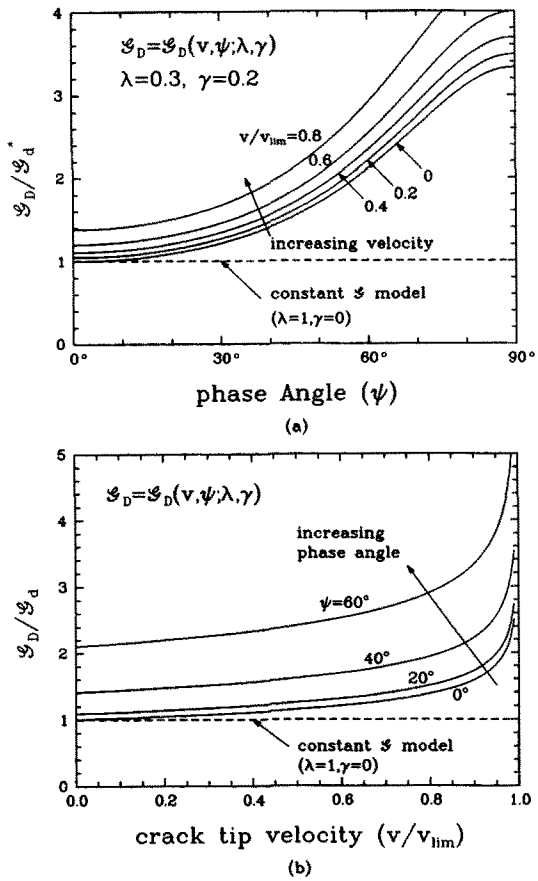

Fig. 1. Models for fracture toughness criteria $\mathcal{G}_D(v, \psi; \lambda, \gamma)$ in (17) with $\lambda = 0.3$ and $\gamma = 0.2$. (a) Normalized toughness plotted as a function of phase angle for various crack-tip velocities. (b) Normalized toughness plotted as a function of crack-tip velocity for various phase angles.

between $\mathcal{G}_D$ and v, ψ can also be proposed. The advantage of the above function is that it is simple, physically based, and has the freedom to cover a wide range of possible criteria by changing the parameters λ and γ. The family of curves representing the toughness function for $\lambda = 0.3$ and $\gamma = 0.2$ is shown in Fig. 1. The curves in Fig. 1(a) are plotted as a function of the phase angle for various crack-tip velocities. As the crack-tip velocity increases, the curves shift upward, indicating a greater energy release rate to propagate. The toughness curves in Fig. 1(b) are plotted as a function of crack-tip velocity for various phase angles.

For the dynamic interface crack, the definition of a limiting velocity is rather ambiguous. Yang *et al.* (1991) have reported that the energy release rate is still finite when the crack-tip velocity is equal to the slower Rayleigh wave speed of the two materials. However, they did not discuss the limiting velocity at which the energy flow into the propagating crack becomes infinite. Here, an attempt is made to determine the limiting velocity of interface cracks by computing the energy factor $\mathcal{F}$ in (6). We determine the velocity when this energy factor becomes infinite. Obviously, the limiting velocity depends on the properties of two materials. The limiting velocities are computed for a bimaterial with $\rho_1 = \rho_2$, $\nu_1 = \nu_2 = 0.3$ and various ratios of the Young's modulus. The velocity is normalized by the shear wave speed of slower material c_S^1 and plotted as a function of E_2/E_1 in Fig. 2. For $E_2/E_1 = 1$, we have a homogeneous solid and $v_{lim} = c_R$. As the ratio of stiffness increases, the limiting velocity increases rapidly to the upper bound which is the slower shear wave speed of the two materials ($v_{lim} = c_S^1$). In fact, v_{lim} is within 1% of c_S^1 for $E_2/E_1 > 4$. Thus for all practical purposes, c_S^1 can be approximated as the limiting velocity of most interface cracks. The physical interpretation of the crack-tip field when $v > c_R^1$ is not clear since the oscillatory index ε becomes a complex number in this range.

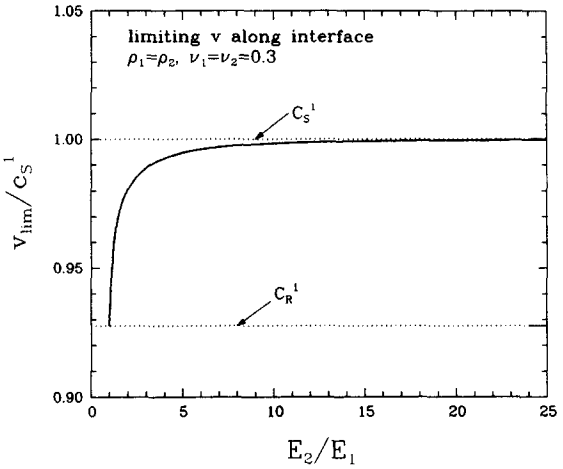

Fig. 2. The limiting velocity of a bimaterial crack tip (determined by $\mathcal{F} \to \infty$) for various ratios of the bimaterial modulus. The velocity is normalized by the shear wave speed of the slower material. The Rayleigh wave of the slower material is indicated for reference. (Note the zero suppression on the ordinate axis.)

3.2. *Contact condition behind the crack tip*

For the energy release rate to be the characterizing parameter in linear elastic materials, the moving crack tip must be surrounded by the mixed-mode K-field. However, in general, the contact of upper and lower crack surfaces behind the interface crack tip exists when $\varepsilon \neq 0$. In the vicinity of the contact zone, the K-field solution (11) cannot be valid. The existence of a K-field can be examined by studying the displacement jump across the crack surface ($\theta = \pm\pi$). The estimated displacements can be obtained from the dynamic interface K-field solution as

$$\delta_2 + i\eta\delta_1 = \frac{2H_{22}|\mathbf{K}L^{i\varepsilon}|}{\sqrt{1+4\varepsilon^2}\cosh\pi\varepsilon}\sqrt{\frac{r}{2\pi}}\,e^{i[\psi(L)-\tan^{-1}(2\varepsilon)+\varepsilon\ln(r/L)]}, \tag{18}$$

where δ_1 and δ_2 are the opening displacements in the x_1 and x_2 directions behind the crack tip, respectively. The characteristic length L is used here to define ψ. The contact of the upper and lower crack surfaces occurs when $\delta_2 \leqslant 0$. Based on the above equation, this condition takes place when $\varepsilon \neq 0$ regardless of the magnitudes of stress intensity factors. If the contact region is sufficiently small so that the K-dominated region exists outside such a region, then the stress intensity factors can still be regarded as the characterizing parameters for the crack-tip field.

It is useful to estimate the size of the contact region for dynamically propagating interface cracks. If the size of the contact region is denoted by r_c, then the estimate for the contact size (Rice, 1988) can be made from the displacement jump (18) as

$$r_c = L\exp\left[\frac{-\pi/2-\psi(L)+\tan^{-1}(2\varepsilon)}{\varepsilon}\right]. \tag{19}$$

In the above equations, the denominator ε indicates that r_c increases exponentially as ε increases. Note that r_c is independent of the magnitude of $\mathbf{K}$ but it does depend on the velocity through the value of ε. In the static case, the contact zone size depends on both the material mismatch and loading conditions. Usually ε is small so that the contact zone is confined to the region close to the tip unless a relatively large shear deformation exists. However, in the dynamic case, ε can be large under high crack-tip speed. In fact, ε becomes unbounded when the crack-tip velocity approaches the limiting velocity, v_{lim}. Suppose $r_c/L < 0.01$ is chosen as the condition for the existence of the K-field (i.e. small contact zone), then $\psi(L)$ must satisfy the following conditions:

$$-\frac{\pi}{2}+\tan^{-1}(2\varepsilon)+4.6\varepsilon<\psi(L)<\frac{\pi}{2}+\tan^{-1}(2\varepsilon). \tag{20}$$

For example, if we consider two materials with $E_2/E_1 = 5$, $\nu_1 = \nu_2 = 0.3$, $\rho_1 = \rho_2$, then for $v/c_S^1 = 0.6$, $\varepsilon = 0.0989$ and the estimated contact zone size is $r_c/L = 9.2\times10^{-7}$ when $\psi(L) = 0°$ (see results of Section 5). The allowable range of the phase angle can be determined from (20) as $-53° < \psi(L) < 101°$. For cases with $\varepsilon < 0$, ε changes $-\varepsilon$ and $\psi(L)$ changes $-\psi(L)$ in both (19) and (20). We emphasize that the above condition is a simple approximation and the actual requirement for the existence of the K-field is probably more restrictive since the size of the K-dominated field for a moving crack is much smaller than the static case (Freund and Rosakis, 1992).

4. COMPUTATIONAL PROCEDURE

4.1. *Domain integral form*

The fundamental crack-tip integral for the energy release rate (1) as well as the interaction integral (5) are given in terms of the limiting field or the near tip quantities. From a discrete computational point of view, these expressions are not suitable for evaluating $\mathcal{G}$ and I since the precise numerical evaluation of the limiting fields is difficult. An accurate procedure based on the "domain integral formulation" is adopted here. In the formulation, we use a weighting function q to transform these path integrals to an area/domain integral. The derivation is similar to the one shown for the static case in Shih and Asaro (1988). With the use of the divergence theorem and the equation of motion, the domain integral form of $\mathcal{G}$ is

$$\mathcal{G} = \int_A \left[\sigma_{ij}\frac{\partial u_i}{\partial x_1}\frac{\partial q}{\partial x_j} - (W+T)\frac{\partial q}{\partial x_1} + \rho\left(\frac{\partial^2 u_i}{\partial t^2}\frac{\partial u_i}{\partial x_1} - \frac{\partial u_i}{\partial t}\frac{\partial^2 u_i}{\partial x_1 \partial t}\right)q\right] \mathrm{d}A, \tag{21}$$

where A is the domain enclosed by the path Γ and crack surfaces. For the interaction integral, it is

$$I = \int_A \left[\left(\sigma_{ij}\frac{\partial u_i^{\text{aux}}}{\partial x_1} + \sigma_{ij}^{\text{aux}}\frac{\partial u_i}{\partial x_1}\right)\frac{\partial q}{\partial x_j} - \left(\sigma_{ij}\varepsilon_{ij}^{\text{aux}} + \rho\frac{\partial u_i}{\partial t}\frac{\partial u_i^{\text{aux}}}{\partial t}\right)\frac{\partial q}{\partial x_1}\right.$$

$$\left. + \rho\left(\frac{\partial^2 u_i}{\partial t^2}\frac{\partial u_i^{\text{aux}}}{\partial x_1} + \frac{\partial^2 u_i^{\text{aux}}}{\partial t^2}\frac{\partial u_i}{\partial x_1} - \frac{\partial^2 u_i}{\partial x_1 \partial t}\frac{\partial u_i^{\text{aux}}}{\partial t} - \frac{\partial u_i}{\partial t}\frac{\partial^2 u_i^{\text{aux}}}{\partial x_1 \partial t}\right)q\right] \mathrm{d}A. \tag{22}$$

The weighting parameter q is a smooth function of x_1, x_2 and has a value of zero on Γ and unity at the crack tip. The domain integral expressions are implemented in post-processing programs to evaluate $\mathcal{G}$ and I. For the auxiliary solutions, we used the asymptotic solutions of a steady-state interface crack given by Yang *et al.* (1991). We derived the explicit expressions of their displacement gradients and they are in the Appendix.

In order to compute $\mathcal{G}$ and I, 5 to 6 domains enclosing up to 500 elements are typically chosen. The locations of the domains must move with the crack tip as it propagates through the interface. The variations of $\mathcal{G}$ from different domains are used to check the accuracy of the solutions.

4.2. *Simulation of crack propagation*

A number of techniques exist for simulating crack propagation in the finite element analysis. Here, the "node release technique" is adopted. The advantage of this technique is that it requires no special type of element or remeshing of the model at every increment. Thus, any existing or commercially available finite element codes can be used. We tailored

the node release procedure for the dynamic interface crack analysis and the brief description is given below.

Two key points separate the current procedure from the usual dynamic crack propagation in a homogeneous material. First, both upper and lower planes of the crack must be modeled since the symmetry condition never exists in the interface crack model. Unlike the symmetrical case where a simple release of the prescribed boundary condition at a node is carried out, the bimaterial crack requires two sets of nodes, one belonging to the upper plane and the other belonging to the lower plane, to be placed along the interface. Initially they are constrained to displace together until the crack tip reaches the node location. At this time, the constraint holding the two nodes is removed and equivalent forces are applied to hold them together. The magnitude of forces are determined from the net force through these nodes. Unlike the pure Mode I case, the force vectors contain not only the x_2 component but also the x_1 component. It is because the interface crack always has a Mode II contribution. During the crack tip advance through one element length, the magnitudes of these force vectors (total of four components) are gradually reduced to zero over five increments. We have tested with more increments and found five increments per crack-tip advance over an element to be sufficient to obtain accurate results. The amplitude of each force component is reduced linearly with time. At every increment, both $\mathcal{G}$ and I are computed from the field solution and the *average* $\mathcal{G}$ and I over five increments are determined. They are reported as $\mathcal{G}$ and I of the mid-step or when the crack-tip is mid-way. By comparing with the exact solutions of homogeneous cracks, this method of computing $\mathcal{G}$ and I is found to give the most accurate solutions.

4.3. *Iterative scheme for crack propagation*

In the past, most computational simulations of dynamic crack propagation were carried out with a pre-determined crack-tip velocity history. Sometimes, the crack-tip velocity was set constant throughout the propagation or else its variation with time was pre-set with a given record of experimental data. Here, we introduce a new approach to the simulation analysis. This is a stable method and uses an iterative scheme to determine the instantaneous crack-tip velocity. Physically, the velocity is influenced by the current loading condition and a given dynamic toughness criterion. An overview of this method is stated below.

First we assume that the criterion for the crack propagation depends solely on the energy release rate as described in Section 3.1 and the toughness is given as a function of v and ψ. Thus, the condition for the crack propagation is $\mathcal{G} = \mathcal{G}_D(v, \psi)$. Our goal is to match the driving force $\mathcal{G}$ and the criterion $\mathcal{G}_D$ for a given set of v and ψ. But the phase angle ψ cannot be artificially controlled if we assume the crack to remain on the interface during the propagation. Thus, the only variable that may be varied to achieve $\mathcal{G} = \mathcal{G}_D$ is the crack-tip velocity v. Two different approaches may be possible. One is to take many small time increments and use v and ψ from the previous increment to estimate current $\mathcal{G}_D$ and choose appropriate v to get the condition $\mathcal{G} = \mathcal{G}_D$. The disadvantage of the explicit scheme is that the solutions may become very unstable (i.e. the resulting v can be highly oscillatory), especially when the loading is not smooth. The other method is to use larger time increments, but iterate on v till the condition $\mathcal{G} = \mathcal{G}_D$ is satisfied. This implicit scheme produces more stable solutions and is the better of the two under general loading conditions.

We implemented the latter iterative scheme with the node release technique in our analysis. The scheme is also applicable to other techniques such as node shifting, moving crack-tip elements, etc. We note that the explicit scheme is unsuited for the node release technique since the smallest time increment is limited by the lengths of the crack-tip elements. As described in the node release procedure earlier, the time for the crack to advance over an element must be set before the start of each release. This requires the crack-tip velocity of the step to be known *a priori* so that we can input the time interval for the step. During the iterations, we try to obtain the optimum velocity or the suitable time increment so that the resulting $\mathcal{G}$ is equivalent to the dynamic fracture toughness $\mathcal{G}_D$. (Note that varying the time increment changes not only $\mathcal{G}$ but also $\mathcal{G}_D$ since v and ψ change.)

For advancing the crack tip over an element length, the following procedure is taken. Suppose the average crack-tip velocity over the nth advance is estimated as v_n, then any difference or error between $\mathcal{G}$ and $\mathcal{G}_D$ is,

$$f(v_n) = \mathcal{G} - \mathcal{G}_D(v_n, \psi_n). \tag{23}$$

Here ψ_n is an implicit function of v_n since the value of the phase angle cannot be directly controlled. Our goal is to find a suitable v_n with the resulting ψ_n which minimizes the error function $f(v_n)$. For this operation, we use the "secant iteration method" to find the optimum v_n. This method is used here instead of the usual Newton method because the derivative of $f(v_n)$ is not known explicitly.

The iterations are continued until the convergence is achieved. During the $(k+1)$th iteration of nth advance, the velocity based on the secant method is computed as

$$v_n^{k+1} = v_n^k + \frac{(v_n^{k-1} - v_n^k) f(v_n^k)}{f(v_n^k) - f(v_n^{k-1})}. \tag{24}$$

For each iteration, a complete process of the node release (discussed in Section 4.2) through the same set of crack-tip elements is repeated (i.e. each iteration requires five increments of finite element calculations). This is necessary because the dynamic energy release rate and the phase angle are obtained only after the crack-tip traverses an element length. As the new velocity is predicted by (24), the finite element program restarts from the end of the last converged $(n-1)$th advance and repeats the whole node release procedure. The convergence occurs when the computed $\mathcal{G}_n^k$ satisfies the following condition:

$$|\mathcal{G}_n^k - \mathcal{G}_D(v_n^k, \psi_n^k)| / \mathcal{G}_n^k < \text{TOL}, \tag{25}$$

where $\mathcal{G}_n^k$ is the energy release rate of the kth iteration for the nth advance with the trial crack-tip velocity v_n^k. In the analysis, we have set the tolerance level to TOL = 0.01. Since $f(v)$ is not known explicitly, (24) can only be used after the second iteration is over. For the first iteration, the crack-tip velocity from the previous advance is used as the initial guess (i.e. $v_n^1 = v_{n-1}$). For the second iteration, the velocity v_n^2 is determined by combining v_n^1 with a simple function $\alpha(f_n^1)$. For example, if $f(v_n^1)$ is positive, it indicates the crack-tip velocity is lower than the equilibrium state. Then, v_n^2 is increased (i.e. $\alpha(f_n^1) > 1$), so that the resulting energy release rate will be smaller. The amount of velocity increase over v_n^2 is determined from the magnitude of $f(v_n^1)$. If the convergence is not achieved by the second iteration, (24) is used to predict the velocity in the subsequent iterations. When the predicted crack-tip speed becomes very small, the program assumes the crack is arrested and the node release is halted. Only when the driving force $\mathcal{G}$ surpasses $\mathcal{G}_D(v = 0, \psi)$ at a later time, is the node release procedure resumed. For the class of problems analysed here, the convergence is achieved typically within 3–4 iterations, or 15–20 total number of increments per advance. The rate of convergence primarily depends on two factors: the smoothness of the $\mathcal{G}_D(v, \psi)$ function and the rate of loading to the crack-tip region.

The complete flow chart of this iterative crack advance scheme is shown in Fig. 3. Also the node release step is depicted in the figure. Any other techniques (e.g. node shifting) can be implemented in this scheme by replacing the node release step with an appropriate procedure. Since secant method shown here does not require an explicit knowledge of derivatives of $\mathcal{G}$ and $\mathcal{G}_D$ with respect to v, any crack growth criteria $\mathcal{G}_D$ can be applied to this iterative scheme.

5. A FINITE CRACK IN AN INFINITE MEDIUM

5.1. *Computational model*

For the first study of the dynamic crack moving along the bimaterial interface to extract stress intensity factors, a finite crack with its initial length $2a_0$ resting on the interface

FLOW CHART FOR CRACK ADVANCE SCHEME

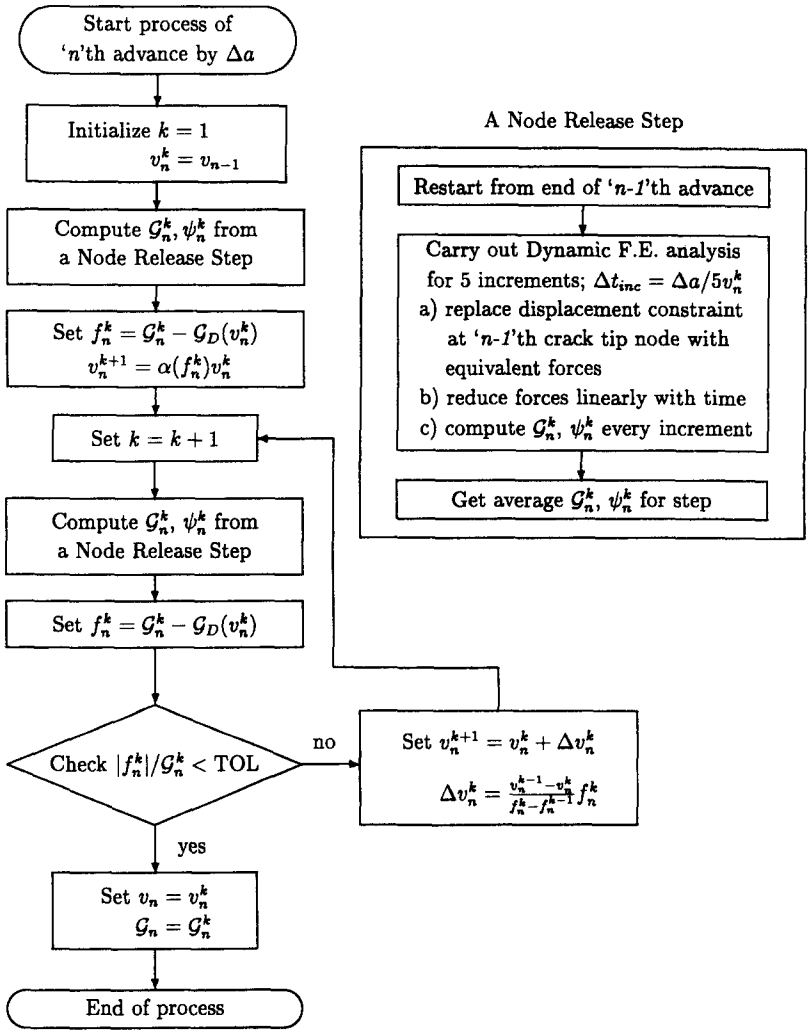

Fig. 3. Flow chart of the iterative scheme used to advance the crack tip. A procedure for node release is also shown.

of two infinitely large isotropic solids is considered. The crack contains two tips and is subjected to either a remote tensile load σ_∞ or a remote shear load τ_∞. At a certain time, $t = 0$, two crack tips begin to propagate simultaneously in opposite directions. It is assumed that the velocity is constant and the crack remains along the interface all the time. The geometry and loading conditions are shown in Fig. 4.

We have tested three different sets of bimaterial properties. For simplicity, we choose Poisson's ratios and the mass densities of the upper plane (material 1) and the lower plane (material 2) to be always the same at $\nu = 0.3$ and $\rho = 1.3461$, respectively. Only the ratio of Young's moduli is changed as (1) $E_2/E_1 = 1$ (homogeneous case), (2) $E_2/E_1 = 5$, (3) $E_2/E_1 = 25$ for the three cases. The static oscillatory index for the interface crack cases is $\varepsilon = 0.0614$ for (2) and $\varepsilon = 0.0860$ for (3). Our primary interest for this analysis is to determine the dynamic stress intensity factors during a transient state and to investigate how the phase angle changes as the crack propagates under a remote loading condition.

In the model, we set the crack with initial length $2a_0$ to lie on the x_1-axis and the origin of the Cartesian coordinates to be at the mid-point of the crack. The half-width and half-height of the model are chosen to be $W/a_0 = 40$ and $H/a_0 = 40$, respectively. These dimensions are large enough so that waves generated from the crack propagation do not

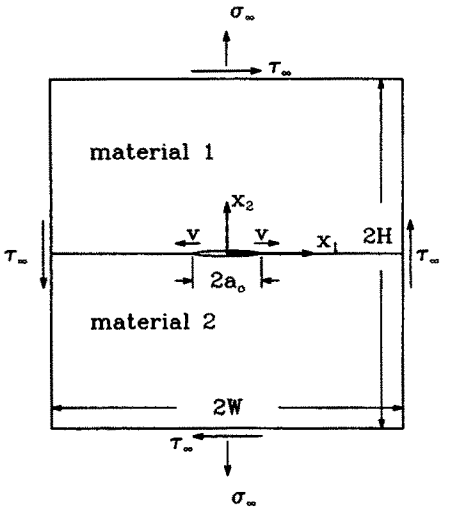

Fig. 4. Schematic of a large plane strain bimaterial plate containing an interface crack with an initial length $2a_0$. Material 2 is always stiffer than or equal to Material 1. The plate is subjected to either remote tension or shear. Propagation of both crack tips is assumed to occur simultaneously with the same velocity.

reach back to the crack tip after they are reflected at the outer boundaries during the time interval of interest. This condition is required for the simulations of crack propagation in an infinite plane.

Two types of loading conditions are considered. One is pure tension and the other is pure shear. With a proper weighting of the solutions from these two conditions, one can determine solutions of any other loading conditions. For the tensile case, a symmetry condition exists across the x_2-axis and only a half of the model needs to be modeled. However, a full model is needed for the shear loading case since no symmetry exists. In constructing the finite element mesh, special care has been taken to design the mesh to maximize the accuracy with the available computational resource. The mesh of the full model shown in Fig. 5 contains 2944 four-node linear elements. The linear type of element is used since higher order elements are not well suited for the node release method. Very small elements are placed near the crack and element sizes are gradually increased with the distance from the crack. Along the boundaries of different sized elements, the displacement constraint is imposed so that the continuity requirements are not violated. Additionally, the ratios of any adjacent element sizes are kept, at most, to four to minimize possible spurious wave reflections at the element boundary. In the vicinity of the crack, the element

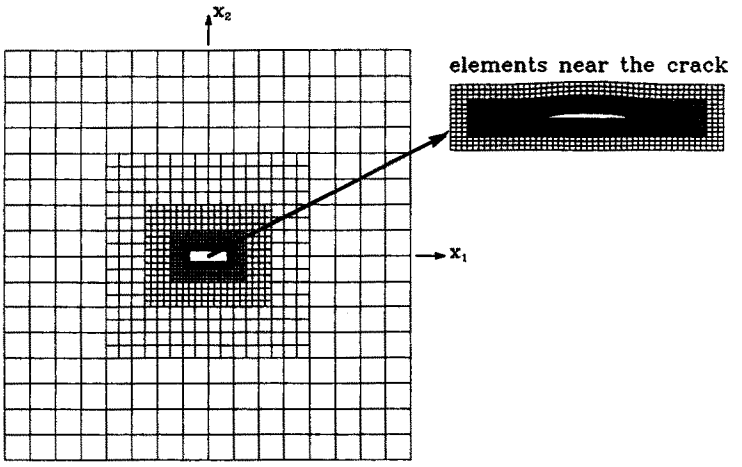

Fig. 5. Finite element mesh of the bimaterial plate. The elements near the crack are enlarged.

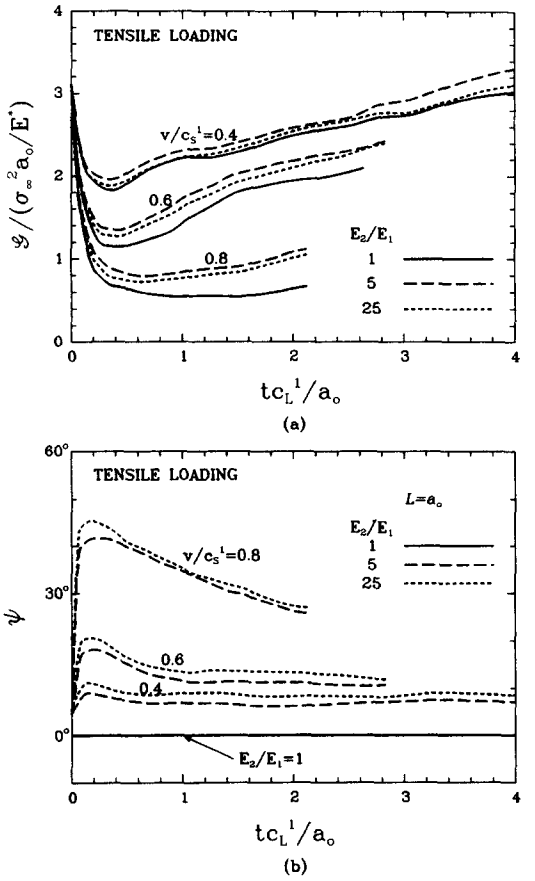

Fig. 6. The results under tensile loading for various crack tip velocities and bimaterial properties as a function of normalized time after the initiation; (a) the normalized dynamic energy release rate, (b) the phase angle with $L = a_0$.

size is chosen to be $a_0/16$. The computations are carried out for at least 20 node release steps, or the equivalent of $\Delta a > 1.2a_0$. We note that the fracture parameters of the first few node releases are not very accurate due to the highly transient nature of the crack-tip field.

Three different crack velocities are chosen for the analysis. They are $v/c_S^1 = 0.4$, 0.6, 0.8 where c_S^1 is the shear wave speed of material 1. For the set of material properties chosen here, the wave speeds of material 1 are always less than those of material 2 except for the case (1) when both materials are identical. Since the crack-tip velocities are pre-set, the iterative scheme discussed in Section 4.3 is not used here. Using the domain integral forms (21), (22), $\mathcal{G}$ and I are computed at every increment. The two values of I obtained with two different auxiliary solutions are used to determine K_I and K_{II}. For expressing the phase angle (13), we choose the half-length of the initial crack (a_0) to be the reference dimension ($L = a_0$).

5.2. *Tensile dominated cases*

Using the symmetry condition across the x_2-axis, only the right half of the finite element mesh (Fig. 5) is used. Initially the plate is loaded by remote tension, σ_∞. Before the crack initiation, the static stress intensity factors are computed with the interaction integral and the results are compared to the exact solutions, $\mathbf{K} = \sigma_\infty\sqrt{\pi a_0}(1+i2\varepsilon)$ (Rice and Sih, 1965). All the results were within a few percent of the exact solutions. The normalized $\mathcal{G}$ before the initiation for the three cases are $\mathcal{G}/(\sigma_\infty^2 a_0/E^*) \simeq 3$ (note that E^* is different for each case). In general, the dynamic energy release rate drops immediately following the crack growth initiation then gradually increases [except for the case (1) with $v/c_S^1 = 0.8$] as shown in Fig. 6(a). The drop in $\mathcal{G}$ is consistent with the analytical solution of homogeneous material where the dynamic stress intensity factor is given as $K_I(vt, v) = k(v)K_I(vt, 0)$. Here

$k(v)$ is the universal function which relates the static K_I to the dynamic K_I [see Freund (1990) for details). The universal function vanishes as the crack-tip speed approaches the Rayleigh wave speed (i.e. $k(c_R) = 0$)]. We also observe that when the energy release rate is normalized by $\sigma_\infty^2 a_0/E^*$, the differences among the various bimaterial combinations are small while $\mathcal{G}$ is much more sensitive to the crack-tip velocity. In the figure, the elapsed time after the initiation is normalized by the initial half-length of the crack a_0 and the longitudinal wave of material 1.

For the homogeneous crack case (1) under tensile loading, the crack-tip field consists of a pure Mode I field and the phase angle is always zero regardless of the velocity as shown in Fig. 6(b). For the interface crack cases (2) and (3), K_I and K_{II} are both non-zero since the material mismatch creates the mixed mode condition near the tip. Their initial phase angles are $\psi \simeq 7°$ for the case (2) and $\psi \simeq 9°$ for the case (3) when the characteristic length is taken as $L = a_0$. The figure indicates a sharp rise in ψ and gradual decrease afterward for those cases. At the high speed ($v/c_S^1 = 0.8$), the angle increases as much as 45°. Although not shown here, K_{II} decreases gradually after the initial increase while K_I continues to increase with time. Except for case (1), the behaviors of phase angle for both interface crack cases are very similar as long as their crack-tip velocities are the same. It appears that the difference in phase angles from various crack-tip velocities narrows as the steady-state condition ($t \to \infty$) is approached.

5.3. *Shear dominated cases*

We have also carried out the analysis under remote shear loading, τ_∞. Again, the static stress intensity factors were computed before the propagation and they were close to the exact solutions. The dynamic energy release and the phase angles for the three cases with three different crack-tip velocities were determined. The whole model shown in Fig. 5 is used for the shear case. In addition, the crack advance is carried out at both ends of the crack (i.e. the two crack tips traveling in opposite directions with the same speed). In the analysis, we computed $\mathcal{G}$ (also K_I and K_{II}) at both crack tips to make sure they are identical to each other.

The behavior of $\mathcal{G}$ as shown in Fig. 7(a) is similar to the one under tensile loading. The initial drop is followed by the gradual increase. The phase angle also shows the sharp change and gradual decrease in Fig. 7(b). All the results tend to the corresponding static values as the time progresses. For case (1), the phase angle remains $\psi = 90°$.

5.4. *Combined loading and small contact condition*

The results of tensile and shear loading conditions can be used as basic solutions for determining the energy release rate and the phase angle under general or mixed loading conditions. Suppose remote loading is given by the tensile stress $m_t\sigma_\infty$ and the shear stress $m_s\tau_\infty$ where m_t and m_s are the multiplier coefficients and σ_∞ and τ_∞ are the positive reference loading magnitudes. Then the dynamic energy release rate under combined loading is

$$\mathcal{G}(t) = m_t^2\mathcal{G}_t(t) + m_s^2\mathcal{G}_s(t) + 2m_t m_s\sqrt{\mathcal{G}_t(t)\mathcal{G}_s(t)}\cos[\psi_t(t) - \psi_s(t)]. \tag{26}$$

Here $\mathcal{G}_t(t)$ and $\mathcal{G}_s(t)$ are the energy release rates under the reference tensile σ_∞ and shear τ_∞ loading conditions. Also $\psi_t(t)$ and $\psi_s(t)$ are the phase angles under reference load σ_∞ and τ_∞, respectively. These results are obtained in the previous sections and shown in Figs 6 and 7. Typically, the third term on the right-hand side of (26) is very small since $|\psi_t - \psi_s|$ is close to $\pi/2$, and thus this term can be ignored. In fact under the static condition, it is always $\pi/2$. By taking $|\psi_t - \psi_s| = \pi/2$, the phase angle under combined loading can be simply determined as

$$\psi(t) = \tan^{-1}\left\{\frac{m_s\tau_\infty}{\eta m_t\sigma_\infty}\right\} + \psi_t(t). \tag{27}$$

Here η is the previously introduced traction resolution factor. We can also use these results

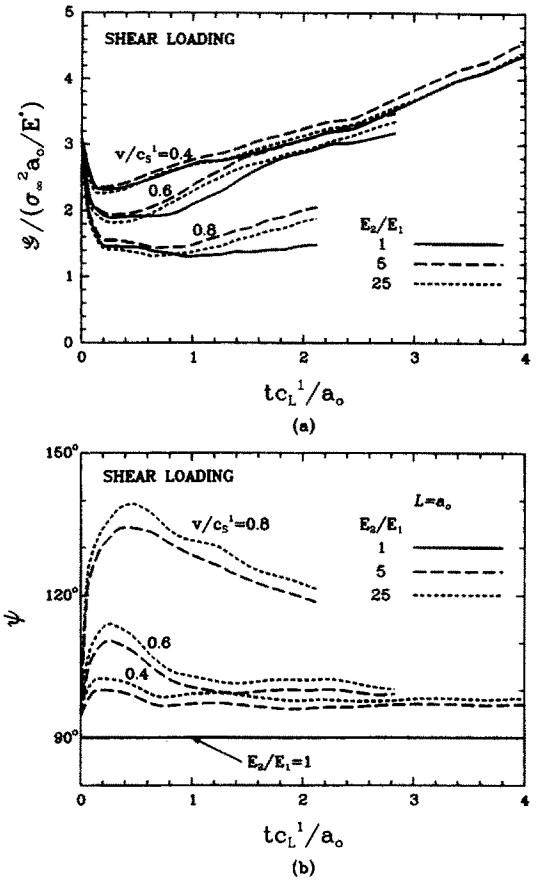

Fig. 7. The results under shear loading for various crack-tip velocities and bimaterial properties as a function of normalized time after the initiatiation; (a) the normalized dynamic energy release rate, (b) the phase angle with $L = a_0$.

to find the contact condition discussed in Section 3.2. Under combined loading, there must be sufficient tensile loading to open up the crack faces to avoid a large contact region behind the crack tip. For case (2) ($E_2/E_1 = 5$) with $v/c_S^1 = 0.6$, the small contact condition (necessary for the K-dominance) requires $m_t > 0$ and the ratio of remote shear to tensile load to be

$$\left|\frac{m_s\tau_\infty}{m_t\sigma_\infty}\right| < 2.0 \quad \text{when } m_s < 0,$$
$$\left|\frac{m_s\tau_\infty}{m_t\sigma_\infty}\right| < 9.5 \quad \text{when } m_s > 0. \tag{28}$$

As stated earlier, the region of K-dominance gets smaller as the crack-tip velocity increases (Freund and Rosakis, 1992), and the requirement of small contact is probably more restrictive.

6. SIMULATIONS OF DYNAMIC INTERFACE CRACK TESTING

6.1. *Computational model*

A limited number of experiments have been conducted to measure the dynamic response of interface cracks. The only data available to us is the work of Tippur and Rosakis (1991) where they conducted an experiment using the CGS (Coherent Grading Sensing) technique to measure deformation fields near the growing crack tip. Using the static

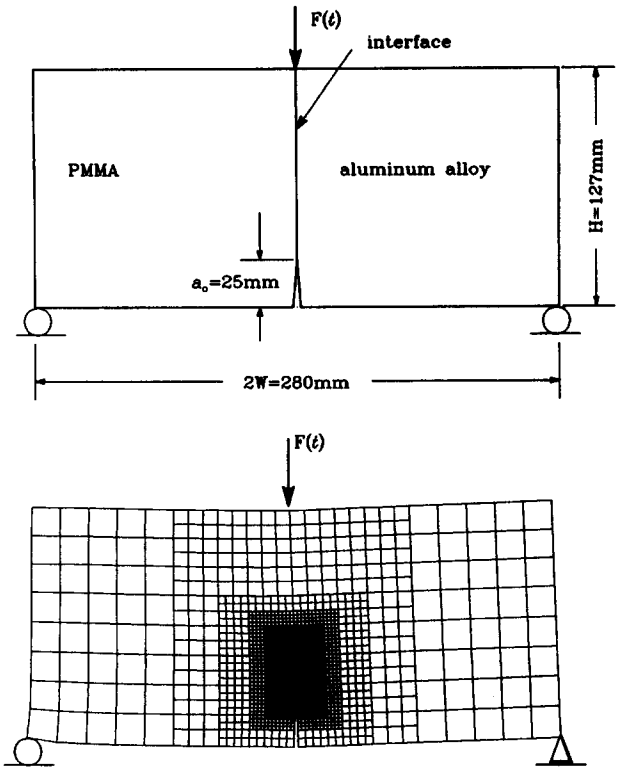

Fig. 8. (a) Schematic of the 3-point bend specimen used by Tippur and Rosakis (1991) for the dynamic interface testing. The impact occurs at the mid-span of the specimen. (b) Plane stress finite element model of the 3-point bend specimen.

asymptotic interface crack-tip field, they obtained the initiation toughness of the interface crack along PMMA and aluminum alloys under an impact loading condition. After the initiation, they were unable to measure the dynamic $\mathcal{G}$ of the propagating interface crack. However, they recorded the accurate crack-tip velocity history during the propagation. We have chosen their model to simulate the dynamic crack growth and to implement the iterative scheme discussed in Section 4.3.

Figure 8 shows the PMMA/aluminum bimaterial specimen in the three-point-bend configuration. In the experiment, the specimen was loaded to fracture by means of the drop weight impacting at the mid-span of specimen. The thickness of the plate is 9 mm. A notch of initial length $a_0 = 25$ mm was cut through the interface after two materials were bonded together.

We have constructed a finite element mesh using 2412 four-noded elements, as shown in Fig. 8. In carrying out the analysis, we have assumed the plane stress condition, which is also the approximation made by Tippur and Rosakis (1991). The length of the elements in the vicinity of the crack is chosen to be $a_0/25$. The element sizes are increased in relation to their distances from the crack. We used the material properties reported by Tippur and Rosakis (1991). They are $E_1 = 3.24$ GPa, $\nu_1 = 0.35$, $\rho_1 = 1{,}200$ kg m^{-3}, $c_L^1 = 1000$ m s^{-1} and $c_S^1 = 2080$ m s^{-1} for PMMA. For the aluminum alloy, they are $E_2 = 80$ GPa, $\nu_2 = 0.3$, $\rho_2 = 2700$ kg m^{-3}, $c_L^2 = 3380$ m s^{-1} and $c_S^2 = 6320$ m s^{-1}. Since the load history was not recorded, the loading is assumed to be a linear function of time (i.e. $F(t) = \Lambda t$, where Λ is a constant). The load is continued to be raised throughout the time span of computation. To find an appropriate rate of loading, we carried out an initial computation to obtain the dynamic energy release rate for the stationary crack. In a typical experiment carried out by Tippur and Rosakis (1991), the crack initiation occurred approximately 90 μs after the load impact (Rosakis, 1992), and measured dynamic initiation toughness was about $\mathcal{G}_D = 150$ N m^{-1}. To match this energy release rate at $t = 90$ μs in our computations, the loading rate is set at $\Lambda = 6700$ MN s^{-1}.

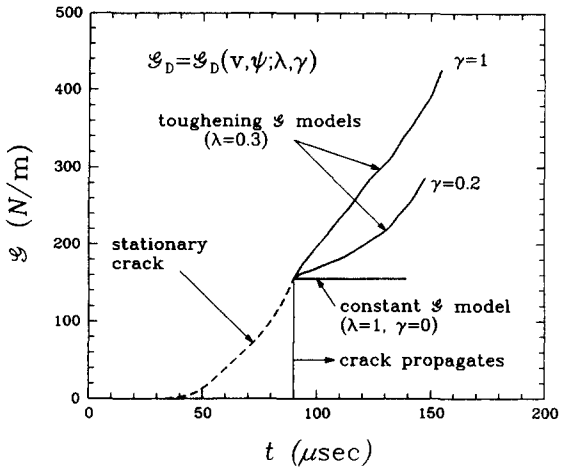

Fig. 9. Energy release rate as a function of time. The dashed line is for $\mathcal{G}$ of the stationary crack. The crack initiates at $t = 90$ μs. The dynamic $\mathcal{G}$ of the propagating crack is shown for three different toughness criteria; a constant $\mathcal{G}$ model with $\lambda = 1$ and $\gamma = 0$, two toughening $\mathcal{G}$ models ($\lambda = 0.3$) with $\gamma = 0.2$ and $\gamma = 1$.

Since the phase angle varies with the characteristic length L and is an important parameter in the toughness formula (17), the choice of L must be made carefully. A different value of L would change the resulting crack-tip velocity as well as the energy release rate and the phase angle. Ideally, the characteristic distance L is set such that $\mathcal{G}_D(\psi)$ at $\psi(L) = 0°$ is the lowest toughness for the interface crack or the toughness curve $\mathcal{G}_D(\psi)$ is symmetric about $\psi(L) = 0°$ (Hutchinson and Suo, 1991). This size is usually the microstructural length scale and its magnitude should be comparable to the size of the K-dominated zone. However, there is no information available for the PMMA/aluminum alloy interface crack, and we choose $L = 100$ μm, which is used by O'Dowd *et al.* (1992) for the alumina/niobium interface crack testing. For setting up the toughness formula (17), $\mathcal{G}_d^*$ is computed from $\mathcal{G}_d^* = \mathcal{G}_D[1+(\lambda-1)\sin^2\psi]$ where $\mathcal{G}_D = 150$ N m^{-1} and $\psi = 22°$ at the initiation ($v = 0$). The limiting velocity is computed as $v_{lim} = 999.6$ m s^{-1} which is essentially identical to c_S^1.

We have carried out the analysis using the proposed dynamic interface toughness criterion (17) to propagate the crack. Instead of carrying the analysis with arbitrary values of λ and γ, we have fixed λ and changed γ to get a good agreement between the resulting velocity and the experimental record of Tippur and Rosakis (1991). Alternatively, one can keep γ constant and change λ to obtain the best approximation. Furthermore, it is possible to carry out a detailed parametric study for various toughening models. However, that is not our purpose here.

For choosing a proper value of λ, we used the result of a static epoxy/glass interface toughness testing, where Hutchinson and Suo (1991) suggested $\lambda = 0.3$ to be the optimum value. We have carried out several computations with $\lambda = 0.3$ and different values for γ. For reference, we also ran the case with $\lambda = 1$ and $\gamma = 0$ which is labeled as a "constant $\mathcal{G}$ model". In this case, the toughness is always constant, independent of the phase angle and the crack-tip velocity (i.e. $\mathcal{G}_D = \mathcal{G}_d^*$). The cases with $\lambda = 0.3$ and $\gamma \neq 0$ are denoted as "toughening $\mathcal{G}$ models" since they require greater $\mathcal{G}$ for increasing values of v and ψ. We note that all of the cases must use the iterative scheme discussed in Section 4.3, including the constant $\mathcal{G}$ model, to determine correct crack-tip history.

6.2. *Computed results*

The linearly increasing load $F(t)$ is applied at the mid-span of the specimen at $t = 0$. After the impact, the compressive stress wave transverses to the crack-tip region. It takes about 40 μs for sizeable loading to build up in the crack-tip region as shown by the dynamic energy release results in Fig. 9. The crack tip remains stationary until $t = 90$ μs when the energy release rate rises to the critical value of $\mathcal{G} = 150$ N m^{-1}. At this time, the crack initiation occurs and the propagation begins. In the propagation phase, three separate

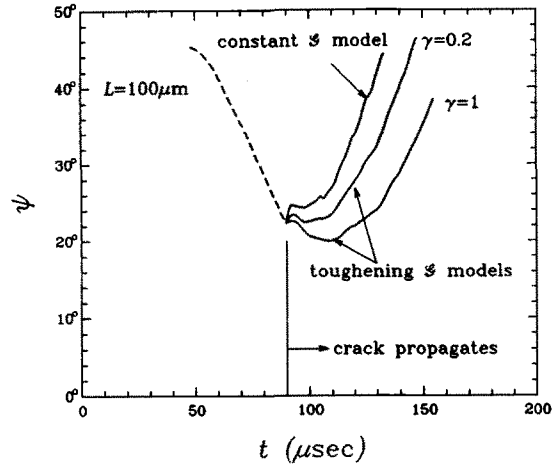

Fig. 10. Phase angle as a function of time. The dashed line is for ψ of the stationary crack. The results of propagating crack is shown for three different toughness criteria.

results are shown in Fig. 9. Two of them are from the toughening $\mathcal{G}$ models ($\lambda = 0.3$) with $\gamma = 1$ and 0.2. Although we have carried out cases with other values of γ, only these results are shown here for clarity. Between these two criteria, the model with $\gamma = 1$ has higher $\mathcal{G}_D$ than that with $\gamma = 0.2$ when v and ψ are the same. The other model on the figure is the constant $\mathcal{G}$ model ($\lambda = 1, \gamma = 0$) where the toughness is always constant regardless of v and ψ. Similar results for the phase angle are shown in Fig. 10. The reason that $\mathcal{G}$ of $\gamma = 1$ has a faster rise with respect to time can be explained from the rate that energy flows into the moving crack tip. All models have the same external loading rate and therefore a similar rate of energy flow available for the crack to propagate which is expressed as $v\mathcal{G}$ (i.e. the product $v\mathcal{G}$ of three models are similar all the time). Since the model with $\gamma = 1$ needs a greater energy release rate to propagate, it has a larger dynamic $\mathcal{G}$ but has a lower crack-tip velocity than the others (see Fig. 11).

The results for the phase angle are shown in Fig. 10. The phase angle during the early period ($t < 40$ μs) is meaningless since there is not sufficient crack-tip loading. In the stationary crack phase, the phase angle starts out with a large value, indicating the presence of larger antisymmetrical or shear deformation. This condition is caused by the different wave speeds for PMMA and aluminum, creating uneven loading across the crack plane. The relative shear steadily decreases as the primary loading tends to that of symmetrical structural bending, as shown by the drop of ψ in Fig. 10. This trend reverses once the crack initiation occurs at $t = 90$ μs. The rapidly propagating crack tip generates large

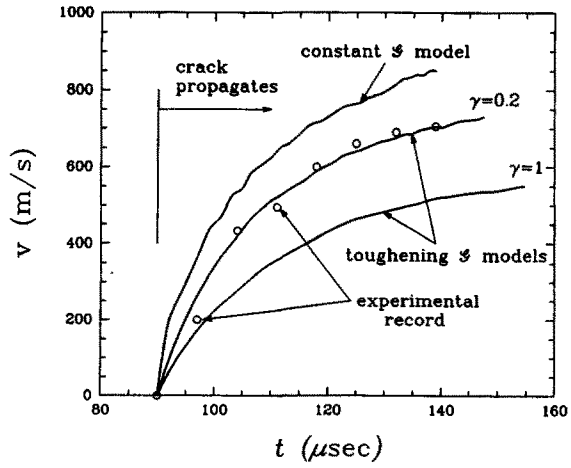

Fig. 11. The resulting crack-tip velocity after the initiation for three different toughness criteria. The experimental data of Tippur and Rosakis (1991) are also shown with circles.

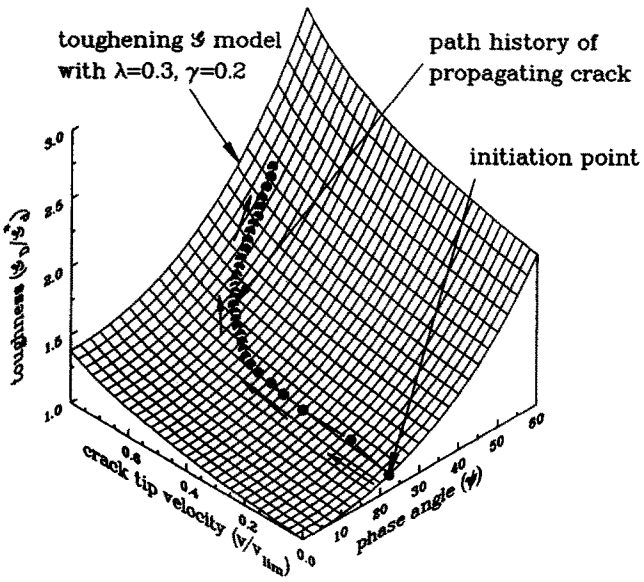

Fig. 12. Toughness surface of dynamic interface crack defined by ψ and v space given in (17) for $\lambda = 0.3$ and $\gamma = 0.2$. The path taken by the propagating crack in the simulation is shown on the surface. (Note the zero suppression on the toughness axis.)

antisymmetrical deformation and the phase angle increases. The increase is largest for the constant $\mathcal{G}$ model since it has the highest crack-tip velocity. As observed in the previous analysis, a larger v yields greater ψ.

The crack-tip velocity after the initiation is shown in Fig. 11. As described earlier, the constant $\mathcal{G}$ model has the largest v. Since this criterion requires no increase in $\mathcal{G}$, the crack tip continues to accelerate. The maximum velocity attained by this model at the end of computation is very close to the Rayleigh wave speed of PMMA, $c_R^1 = 930$ m s^{-1}. On the other hand, the resistance for fracture increases for the toughening $\mathcal{G}$ models as the crack tip increases its speed. Since the model with $\gamma = 1$ has a greater resistance to the crack propagation, it has the lowest velocity history. In Fig. 11, the experimental data obtained by Tippur and Rosakis (1991) is also shown with circles. As described earlier, we have varied the value of γ to match the resulting crack-tip velocity to the experimental observation. After trying a few different values, we have determined that the combination of $\gamma = 0.2$ and $\lambda = 0.3$ gives the record of v which is in excellent agreement with the experimental data for the *entire* range.

Since the toughness formula (17) is given as a function of v and ψ, one can create a toughness surface of the dynamic interface crack for a given set of λ and γ. Such a surface is shown for $\lambda = 0.3$ and $\gamma = 0.2$ in Fig. 12. If this were a correct criterion, the energy release rate for a given crack-tip velocity and phase angle must always lie on this surface for any crack propagation to occur. In fact, the path history of the propagating crack simulated here is shown with dark circles in the figure. Each circle represents a propagation through an element length. This plot clearly illustrates, starting from initiation at $v = 0$, how the crack tip accelerates and the phase angle increases to attain a large level of $\mathcal{G}$ under an increasing driving force. Alternatively, if the crack driving force is reduced, the path on the surface would reverse its course to a lower level and eventually the crack might arrest ($v = 0$). We have also estimated the size of the contact zone and it ranges from $r_c = 10^{-4}$ to 10^{-1} μm.

7. DISCUSSIONS

In this work, a new conservation integral has been presented for evaluating the characteristics of dynamic crack propagation along bimaterial interfaces. This formulation allows

for the extraction of the independent Mode I and Mode II components from the K-field of the propagating interface crack. When applied to the case of an interface crack in an infinite domain, a very interesting insight into the influence of crack-tip dynamics was observed. The results of the energy release rate and phase angle of the dynamic interface crack show greater sensitivity to the crack-tip velocity than to the modulus mismatch between the two materials. Thus, many conclusions drawn about crack growth behavior for particular bimaterial systems under quasi-static growth conditions may not hold under dynamic crack growth behavior. As the crack-tip speed increases, very rapid growth in the phase angle is observed at early times, followed by a slower decay to a steady-state value which is far less sensitive to crack-tip speed than the early time values.

We have presented a new toughness criterion postulated to govern the growth rate of bimaterial interface cracks. Together with a newly formulated iterative procedure for computing crack propagation, we present results for computations of arbitrary dynamic crack growth along interfaces. We have applied this methodology to simulate experimental results on bimaterial three-point-bend specimens under impact loading conditions. We demonstrate that with a proper choice of parameters, our toughness criterion is able to accurately replicate the experimentally recorded interface crack propagation results. It is to be emphasized that our model involves no "curve fitting" to experimental data. It utilizes a measured initiation toughness and depends on a choice for a proper wave speed for the bimaterial system. The new iterative crack propagation technique implements the toughness criterion and properly releases nodes without any empirical factors.

It is interesting to note that Nakamura *et al.* (1989) have discussed a concept of transition time for the three-point-bend bar under dynamic load. The transition time marks a shift from when the stress field around the crack tip is dominated by stress waves transient to a field controlled more by the structural inertia of the deforming beam. The transition time is also used to measure the stability of the K- or J-dominated crack-tip field. This is a necessary condition if K or $\mathcal{G}$ is used as the critical parameter for the dynamic crack initiation. Applying the formula given for a homogeneous material (Nakamura *et al.*, 1989), we find the transitional time to be $\sim 25\ \mu s$ for aluminum and $\sim 80\ \mu s$ for PMMA with given dimensions of the specimen. Although the precise transition time for the bimaterial specimen cannot be determined without more detailed study, it is likely that the crack initiation time (90 μs) observed by Tippur and Rosakis (1991) is longer than the transition time.

Simulations such as we have presented should help to provide critical insight into the proper interpretation of experimental data for dynamic interface cracks. Instead of applying a proposed toughness formula, one can also use the experimental record of the crack-tip velocity to propagate the crack. However, as shown by various results in this paper, the dynamic energy release rate and the phase angle are very sensitive to the crack-tip velocity. Thus, computed $\mathcal{G}$ and ψ may not be accurate unless precise measurements of the crack-tip velocity are given at small time intervals. Therefore, in general, varying the toughness criterion to match the resulting velocity well with the experimental data is probably an optimum approach. In this manner the dominant crack-tip field parameters associated with measured crack-tip growth rates are predicted and can be used to interpret the measured correlation between loading and crack-tip velocity. Though the present work only deals with an interface crack between isotropic materials, an orthotropic material model can be incorporated in the procedures shown here. This work is currently in progress.

Acknowledgements—The authors gratefully acknowledge the support of ONR under Grant No. N0001491J1352. Computations were performed on VAXstations. The finite element analysis was carried out with the ABAQUS code, which was made available under academic license from Hibbitt, Karlson and Sorenson, Inc., Providence, RI.

REFERENCES

Freund, L. B. (1990). *Dynamic Fracture Mechanics*. Cambridge University Press, Cambridge.

Freund, L. B. and Rosakis, A. J. (1992). The structure of the near tip field during transient elastodynamic crack growth. *J. Mech. Phys. Solids* **40**, 699–719.

Hutchinson, J. W. and Suo, Z. (1991). Mixed mode cracking in layered materials. In *Advance in Applied Mechanics* (edited by J. W. Hutchinson and T. Y. Wu), Vol. 29, pp. 63–191. Academic Press, New York.

Kfouri, A. P. (1986). Some evaluations of the elastic T-term using Eshelby's method. *Int. J. Fract.* **30,** 301–315.
Kobayashi, T. and Dally, J. W. (1979). Dynamic photoelastic determination of the á-K relation for 4340 steel. *ASTM STP* **711,** 189–210.
Nakamura, T. (1991). Three-dimensional stress fields of elastic interface cracks. *J. Appl. Mech.* **58,** 939–946.
Nakamura, T. and Lo, C. Y. (1991). Dynamic crack propagation of circumferentially notched bar based on various growth criteria. In *Mechanical Behavior of Material—VI* (edited by M. Jono and T. Inoue), Vol. 4, pp. 457–462. Pergamon Press, Oxford.
Nakamura, T. and Parks, D. M. (1992). Determination of elastic T-stress along three-dimensional crack fronts using an interaction integral. *Int. J. Solids Structures* **29,** 1597–1611.
Nakamura, T., Shih, C. F. and Freund, L. B. (1989). Three-dimensional transient analysis of a dynamically loaded three-point-bend ductile fracture specimen. *ASTM STP* **995,** 217–241.
O'Dowd, N. P., Stout, M. G. and Shih, C. F. (1992). Fracture toughness of alumina/niobium interface: experiments and analysis. *Phil. Mag.* **A66**(6), 1037–1064.
Ravi-Chandar, K. and Knauss, W. G. (1984). An experimental investigation into dynamic fracture: III. On steady state crack propagation and crack branching. *Int. J. Fract.* **26,** 141–154.
Ravichandran, G. and Clifton, R. J. (1989). Dynamic fracture under plane wave loading. *Int. J. Fract.* **40,** 157–201.
Rice, J. R. (1988). Elastic fracture mechanics concepts for interfacial cracks. *J. Appl. Mech.* **55,** 98–103.
Rice, J. R. and Sih, G. C. (1965). Plane problems of cracks in dissimilar media. *J. Appl. Mech.* **32,** 418–423.
Rosakis, A. J. (1992). Private communication to T. Nakamura.
Rosakis, A. J., Duffy, J. and Freund, L. B. (1984). The determination of dynamic fracture toughness of AISI 4340 steel by the shadow spot method. *J. Mech. Phys. Solids* **32,** 443–460.
Shih, C. F. and Asaro, R. J. (1988). Elastic-plastic analysis of cracks on bimaterial interfaces: part I—small scale yielding. *J. Appl. Mech.* **55,** 299–316.
Stroh, A. N. (1962). Steady state problems in anisotropic elasticity. *J. Math. Phys.* **41,** 77–103.
Tippur, H. V. and Rosakis, A. J. (1991). Quasi-state and dynamic crack growth along bimaterial interfaces: a note on crack tip field measurements using coherent gradient sensing. *Exper. Mech.* **31,** 243–251.
Willis, J. R. (1971). Fracture mechanics of interfacial cracks. *J. Mech. Phys. Solids* **19,** 353–368.
Yang, W., Suo, Z. and Shih, C. F. (1991). Mechanics of dynamic debonding. *Proc. R. Soc. Lond.* **433,** 679–697.

APPENDIX: ASYMPTOTIC FIELD FOR DYNAMIC INTERFACE CRACK

The computation of I for the dynamic mixed-mode stress intensity factors requires the auxiliary field whose solutions must be known *a priori*. The only available analytical fullfield solution for the dynamically propagating crack is the asymptotic or the steady-state solution obtained by Yang *et al.* (1991). They have derived the solutions through the application of Stroh's formulation (1962). The in-plane stress, displacement and displacement gradients components can be expressed as

$$\sigma_{1\alpha} = -2\,\mathrm{Re}\,[\mathrm{i}\xi L_{\alpha 1} f_1' + \mathrm{i}\zeta L_{\alpha 2} f_2' + \rho v^2 A_{\alpha\beta} f_\beta'], \qquad \sigma_{2\alpha} = 2\,\mathrm{Re}\,[L_{\alpha\beta} f_\beta'],$$
$$u_\alpha = 2\,\mathrm{Re}\,[A_{\alpha\beta} f_\beta], \qquad u_{\alpha,1} = 2\,\mathrm{Re}\,[A_{\alpha\beta} f_\beta'], \qquad u_{\alpha,11} = 2\,\mathrm{Re}\,[A_{\alpha\beta} f_\beta''], \tag{A1}$$

where the subscripts α and β range 1 to 2, $\xi = \sqrt{1-(v/c_L)^2}$, $\zeta = \sqrt{1-(v/c_S)^2}$ and $(\,)' = \dfrac{\partial}{\partial z_\alpha}$. Stroh's formulation breaks down when $v = 0$ for isotropic materials, but the limiting solutions as $v \to 0$ converge to the corresponding quasi-static solutions. Also $\mathbf{A}$ and $\mathbf{L}$ are the following 2×2 matrices:

$$\mathbf{A} = \begin{bmatrix} 1 & -\mathrm{i}\zeta \\ \mathrm{i}\xi & 1 \end{bmatrix}, \qquad \mathbf{L} = \mu \begin{bmatrix} 2\mathrm{i}\xi & 1+\zeta^2 \\ -(1+\zeta^2) & 2\mathrm{i}\zeta \end{bmatrix}. \tag{A2}$$

The analytic function f_α is

$$f_\alpha(z_\alpha) = \frac{1}{\sqrt{2\pi}} \left[\frac{\mathrm{e}^{\pi\varepsilon} \mathbf{K} z_\alpha^{1/2+\mathrm{i}\varepsilon}}{(1+2\mathrm{i}\varepsilon)\cosh \pi\varepsilon} \mathbf{I}^\alpha \cdot \mathbf{w} + \frac{\mathrm{e}^{-\pi\varepsilon} \bar{\mathbf{K}} z_\alpha^{1/2-\mathrm{i}\varepsilon}}{(1-2\mathrm{i}\varepsilon)\cosh \pi\varepsilon} \mathbf{I}^\alpha \cdot \bar{\mathbf{w}} \right], \tag{A3}$$

where $z_1 = \hat{x}_1 + \mathrm{i}\xi\hat{x}_2$ and $z_2 = \hat{x}_1 + \mathrm{i}\zeta\hat{x}_2$. The coordinates $\hat{x}_\alpha$ translate with the moving crack tip along the x_1-axis. The vector $\mathbf{I}^\alpha$ is the αth row of the inverse matrix $\mathbf{L}^{-1}$, $\mathbf{w} = \frac{1}{2}(-\mathrm{i}\eta, 1)$, $\bar{\mathbf{w}} = \frac{1}{2}(\mathrm{i}\eta, 1)$ and the traction resolution factor η is given in the text.

As shown in (22), explicit forms of stress and displacement gradients must be provided for the computation of I. The domain integral also contains the time derivative of displacement. For the steady-state solutions, the relationship between the spatial and the time derivatives are given as

$$\frac{\partial u_i}{\partial t} = -v \frac{\partial u_i}{\partial x_1} = -v u_{i,1}, \qquad \frac{\partial^2 u_i}{\partial t^2} = -v \frac{\partial^2 u_i}{\partial x_1 \partial t} = v^2 \frac{\partial^2 u_i}{\partial x_1^2} = v^2 u_{i,11}. \tag{A4}$$

The above relationships are used in determining the time derivatives of the displacement. In the following, all the necessary displacements and their gradients are given. Since the components of the asymptotic stress (11) are shown in Yang *et al.* (1991), they are not given here.

The displacement and its gradients in the K-field can be expressed in the following forms:

$$u_i(r,\theta;\varepsilon) = \mathrm{Re}\,[\mathbf{K}r^{i\varepsilon}]\sqrt{\frac{2r}{\pi}}\,\tilde{u}_i^{\mathrm{I}}(\theta;\varepsilon) + \mathrm{Im}\,[\mathbf{K}r^{i\varepsilon}]\sqrt{\frac{2r}{\pi}}\,\tilde{u}_i^{\mathrm{II}}(\theta;\varepsilon),$$

$$u_{i,1}(r,\theta;\varepsilon) = \frac{\mathrm{Re}\,[\mathbf{K}r^{i\varepsilon}]}{\sqrt{2\pi r}}\,\tilde{u}_{i,1}^{\mathrm{I}}(\theta;\varepsilon) + \frac{\mathrm{Im}\,[\mathbf{K}r^{i\varepsilon}]}{\sqrt{2\pi r}}\,\tilde{u}_{i,1}^{\mathrm{II}}(\theta;\varepsilon),$$

$$u_{i,11}(r,\theta;\varepsilon) = \mathrm{Re}\,[\mathbf{K}r^{i\varepsilon}]\sqrt{\frac{2}{\pi r^3}}\,\tilde{u}_{i,11}^{\mathrm{I}}(\theta;\varepsilon) + \mathrm{Im}\,[\mathbf{K}r^{i\varepsilon}]\sqrt{\frac{2}{\pi r^3}}\,\tilde{u}_{i,11}^{\mathrm{II}}(\theta;\varepsilon). \tag{A5}$$

The non-dimensional functions for angular variation are given in the following. First the angular functions $\tilde{u}_i^{\mathrm{I}}(\theta;\varepsilon)$ and $\tilde{u}_i^{\mathrm{II}}(\theta;\varepsilon)$ are

$$\tilde{u}_1^{\mathrm{I}}(\theta;\varepsilon) = \frac{(\mu D\cosh\pi\varepsilon)^{-1}}{\sqrt{1+4\varepsilon^2}}\left\{\xi_s^{1/2}\left(P_{11}\cos\xi_-\cos\frac{\xi_t}{2} - P_{12}\sin\xi_-\sin\frac{\xi_t}{2}\right)\right.$$
$$\left. + \zeta\zeta_s^{1/2}\left(P_{21}\cos\xi_-\cos\frac{\zeta_t}{2} - P_{22}\sin\xi_-\sin\frac{\zeta_t}{2}\right)\right\},$$

$$\tilde{u}_2^{\mathrm{I}}(\theta;\varepsilon) = \frac{(\mu D\cosh\pi\varepsilon)^{-1}}{\sqrt{1+4\varepsilon^2}}\left\{\xi\xi_s^{1/2}\left(P_{11}\cos\xi_-\sin\frac{\xi_t}{2} + P_{12}\sin\xi_-\cos\frac{\xi_t}{2}\right)\right.$$
$$\left. + \zeta_s^{1/2}\left(P_{21}\cos\xi_-\sin\frac{\zeta_t}{2} + P_{22}\sin\xi_-\cos\frac{\zeta_t}{2}\right)\right\},$$

$$\tilde{u}_1^{\mathrm{II}}(\theta;\varepsilon) = \frac{(\mu D\cosh\pi\varepsilon)^{-1}}{\sqrt{1+4\varepsilon^2}}\left\{\xi_s^{1/2}\left(-P_{11}\sin\xi_-\cos\frac{\xi_t}{2} - P_{12}\cos\xi_-\sin\frac{\xi_t}{2}\right)\right.$$
$$\left. + \zeta\zeta_s^{1/2}\left(-P_{21}\sin\xi_-\cos\frac{\zeta_t}{2} - P_{22}\cos\xi_-\sin\frac{\zeta_t}{2}\right)\right\},$$

$$\tilde{u}_2^{\mathrm{II}}(\theta;\varepsilon) = \frac{(\mu D\cosh\pi\varepsilon)^{-1}}{\sqrt{1+4\varepsilon^2}}\left\{\xi\xi_s^{1/2}\left(-P_{11}\sin\xi_-\sin\frac{\xi_t}{2} + P_{12}\cos\xi_-\cos\frac{\xi_t}{2}\right)\right.$$
$$\left. + \zeta_s^{1/2}\left(-P_{21}\,sin\,\xi_-\sin\frac{\zeta_t}{2} + P_{22}\cos\xi_-\cos\frac{\zeta_t}{2}\right)\right\}. \tag{A6}$$

The angular functions $\tilde{u}_{i,1}^{\mathrm{I}}(\theta;\varepsilon)$ and $\tilde{u}_{i,1}^{\mathrm{II}}(\theta;\varepsilon)$ are

$$\tilde{u}_{1,1}^{\mathrm{I}}(\theta;\varepsilon) = (\mu D\cosh\pi\varepsilon)^{-1}\left\{\xi_s^{-1/2}\left(P_{11}\cos\xi_0\cos\frac{\xi_t}{2} + P_{12}\sin\xi_0\sin\frac{\xi_t}{2}\right)\right.$$
$$\left. + \zeta\zeta_s^{-1/2}\left(-P_{21}\cos\zeta_0\cos\frac{\zeta_t}{2} - P_{22}\sin\zeta_0\sin\frac{\zeta_t}{2}\right)\right\},$$

$$\tilde{u}_{2,1}^{\mathrm{I}}(\theta;\varepsilon) = (\mu D\cosh\pi\varepsilon)^{-1}\left\{\xi\xi_s^{-1/2}\left(P_{11}\cos\xi_0\sin\frac{\xi_t}{2} - P_{12}\sin\xi_0\cos\frac{\xi_t}{2}\right)\right.$$
$$\left. + \zeta_s^{-1/2}\left(P_{21}\cos\zeta_0\sin\frac{\zeta_t}{2} - P_{22}\sin\zeta_0\cos\frac{\zeta_t}{2}\right)\right\},$$

$$\tilde{u}_{1,1}^{\mathrm{II}}(\theta;\varepsilon) = (\mu D\cosh\pi\varepsilon)^{-1}\left\{\xi_s^{-1/2}\left(-P_{11}\sin\xi_0\cos\frac{\xi_t}{2} + P_{12}\cos\xi_0\sin\frac{\xi_t}{2}\right)\right.$$
$$\left. + \zeta\zeta_s^{-1/2}\left(-P_{21}\sin\zeta_0\cos\frac{\zeta_t}{2} + P_{22}\cos\zeta_0\sin\frac{\zeta_t}{2}\right)\right\},$$

$$\tilde{u}_{2,1}^{\mathrm{II}}(\theta;\varepsilon) = (\mu D\cosh\pi\varepsilon)^{-1}\left\{\xi\xi_s^{-1/2}\left(-P_{11}\sin\xi_0\sin\frac{\xi_t}{2} - P_{12}\cos\xi_0\cos\frac{\xi_t}{2}\right)\right.$$
$$\left. + \zeta_s^{-1/2}\left(-P_{21}\sin\zeta_0\sin\frac{\zeta_t}{2} - P_{22}\cos\zeta_0\cos\frac{\zeta_t}{2}\right)\right\}. \tag{A7}$$

The angular functions $\tilde{u}_{i,11}^{\mathrm{I}}(\theta;\varepsilon)$ and $\tilde{u}_{i,11}^{\mathrm{II}}(\theta;\varepsilon)$ are

$$\tilde{u}_{1,11}^{\mathrm{I}}(\theta;\varepsilon) = \frac{(\mu D\cosh\pi\varepsilon)^{-1}}{\sqrt{1+4\varepsilon^2}}\left\{\xi_s^{-3/2}\left(P_{11}\cos\xi_+\cos\frac{3\xi_t}{2} + P_{12}\sin\xi_+\sin\frac{3\xi_t}{2}\right)\right.$$
$$\left. + \zeta\zeta_s^{-3/2}\left(P_{21}\cos\xi_+\cos\frac{3\zeta_t}{2} + P_{22}\sin\xi_+\sin\frac{3\zeta_t}{2}\right)\right\},$$

$$\tilde{u}^{I}_{2,11}(\theta;\varepsilon) = \frac{(\mu D\cosh\pi\varepsilon)^{-1}}{\sqrt{1+4\varepsilon^2}}\left\{\xi\xi_s^{-3/2}\left(-P_{11}\cos\xi_+\sin\frac{3\xi_t}{2}+P_{12}\sin\xi_+\cos\frac{3\xi_t}{2}\right)\right.$$
$$\left.+\zeta_s^{-3/2}\left(-P_{21}\cos\xi_+\sin\frac{3\zeta_t}{2}+P_{22}\sin\xi_+\cos\frac{3\zeta_t}{2}\right)\right\},$$

$$\tilde{u}^{II}_{1,11}(\theta;\varepsilon) = \frac{(\mu D\cosh\pi\varepsilon)^{-1}}{\sqrt{1+4\varepsilon^2}}\left\{\xi_s^{-3/2}\left(-P_{11}\sin\xi_+\cos\frac{3\xi_t}{2}+P_{12}\cos\xi_+\sin\frac{3\xi_t}{2}\right)\right.$$
$$\left.+\zeta\zeta_s^{-3/2}\left(-P_{21}\sin\xi_+\cos\frac{3\zeta_t}{2}+P_{22}\cos\xi_+\sin\frac{3\zeta_t}{2}\right)\right\},$$

$$\tilde{u}^{II}_{2,11}(\theta;\varepsilon) = \frac{(\mu D\cosh\pi\varepsilon)^{-1}}{\sqrt{1+4\varepsilon^2}}\left\{\xi\xi_s^{-3/2}\left(P_{11}\sin\xi_+\sin\frac{3\xi_t}{2}+P_{12}\cos\xi_+\cos\frac{3\xi_t}{2}\right)\right.$$
$$\left.+\zeta_s^{-3/2}\left(P_{21}\sin\xi_+\sin\frac{3\zeta_t}{2}+P_{22}\cos\xi_+\cos\frac{3\zeta_t}{2}\right)\right\}, \quad \text{(A8)}$$

where the coefficients P_{ij} are

$$P_{11} = (1+\zeta^2)\cosh\varepsilon(\pi-\xi_t)-2\eta\zeta\sinh\varepsilon(\pi-\xi_t),$$
$$P_{12} = (1+\zeta^2)\sinh\varepsilon(\pi-\xi_t)-2\eta\zeta\cosh\varepsilon(\pi-\xi_t),$$
$$P_{21} = \eta(1+\zeta^2)\sinh\varepsilon(\pi-\zeta_t)-2\xi\sinh\varepsilon(\pi-\zeta_t),$$
$$P_{22} = \eta(1+\zeta^2)\cosh\varepsilon(\pi-\zeta_t)-2\xi\sinh\varepsilon(\pi-\zeta_t). \quad \text{(A9)}$$

The factors in the above equations are

$$\xi_s = \sqrt{1-\left(\frac{v\sin\theta}{c_L}\right)^2}, \quad \xi_t = \tan^{-1}(\xi\tan\theta), \quad \xi_0 = \varepsilon\ln\xi, \quad \xi_\pm = \xi_0 \pm \tan^{-1}2\varepsilon,$$
$$\zeta_s = \sqrt{1-\left(\frac{v\sin\theta}{c_S}\right)^2}, \quad \zeta_t = \tan^{-1}(\zeta\tan\theta), \quad \zeta_0 = \varepsilon\ln\zeta, \quad \zeta_\pm = \zeta_0 \pm \tan^{-1}2\varepsilon. \quad \text{(A10)}$$

Also, $D = 4\xi\zeta-(1-\xi^2)^2$. For determining the values in the upper ($0 \leqslant \theta < \pi$) and lower regions ($-\pi < \theta < 0$), use the appropriate shear modulus, shear and longitudinal wave speeds of the respective material. In the lower plane, π should be multiplied by -1 in (A3) and (A9).